Int. J. Electrochem. Sci., 15 **(2020)** 2987 – 3002, doi: 10.20964/2020.04.11

International Journal of
ELECTROCHEMICAL
SCIENCE
www.electrochemsci.org

Erosion and Passivation of Borated 254 SMO Stainless Steel in Simulated Flue Gas Desulfurization Solution

Muhammad Saqlain Qurashi[1], *Yishi Cui*[1], *Jian Wang*[1*], *Nan Dong*[1], *Jingang Bai*[1,2], *Peide Han*[1,*]

[1] College of Materials Science and Engineering, Taiyuan University of Technology, Taiyuan 030024, China;
[2] State Key Laboratory of Advanced Stainless Steel Materials, Taiyuan 030003, China;
[*]E-mail: wangjian@tyut.edu.cn , hanpeide@tyut.edu.cn

Received: 4 November 2019 / *Accepted:* 15 January 2020 / *Published:* 10 March 2020

Grain boundary erosion and passivation of 254 SMO stainless steel with and without boron were investigated in a medium of simulated flue gas desulfurization (FGD) solution. Electrochemical measurements were carried out using potentiodynamic polarization, electrochemical impedance spectroscopy, and Mott-Schottky analysis to determine the significance of boron addition at different temperatures. After potentiodynamic polarization, microstructures and grain boundary erosion were evaluated at 60 ℃ using scanning electron microscopy (SEM). It was found that the dissolution/erosion of grain boundary is much lower when boron is added. Energy-dispersive X-ray spectroscopy was carried out after SEM to determine the reason of grain boundary erosion of nonborated 254 SMO and compared the passive regions of polarization tests at 60 ℃. Experimental results show that the addition of boron significantly hindered the corrosion rate, pits initiation sites, and passive film dissolution. Deconvolution of peaks obtained from X-ray photoelectron spectroscopy (XPS) and their depth profiles after 60 ℃ passivation confirmed that boron not only stopped the corrosion behavior but also increased the stability and repassivation ability of passive film.

Keywords: Superaustenitic stainless steel; grain boundary erosion; boron effect; corrosion resistance; passive film composition

1. INTRODUCTION

Because of the presence of high alloying elements, 254 SMO superaustenitic stainless steel exhibits a good pitting resistance equivalent number (PREN = w_{Cr} + 3.3 w_{Mo} + 30 w_N) of 43, providing this steel excellent corrosion resistance and strong passive film [1,2]. This steel is used in flue gas desulfurization (FGD) systems, desalination units, nuclear pipelines, incinerators, heat exchangers, and chemical processing units [3,4]. The FGD systems act as the chemical processing units/plants to remove the sulfur dioxides and nitrogen oxides present in the residual or exhaust gases; these gases are very

corrosive and toxic to environment [5]. Temperature and the chemical products of these plants directly affect the corrosion resistance of stainless steel. When the temperature reaches to the condensation point or dew point of the exhaust gases, the sulfur oxides and H_2O present in the gases combine to form highly concentrated sulfuric acid, causing the corrosion of steel surface [6]. Temperature significantly affects the corrosion behavior of materials used to handle FGD condensates with sulfides and halides [7], affecting electrochemical measurements and passivation properties [8]. Other than temperature and acidity, halide concentration and flow velocity of ions are also the reasons of corrosion or dissolution rate in the plants/chambers or chimneys of FGD systems [9].

In such harsh and severe conditions, the corrosion rate or surface deterioration becomes much more aggressive. Transpassive dissolution of metal is closely related to passive film breakdown and localized corrosion, leading to the depletion of alloying elements such as Cr in the film; this makes the passive film more vulnerable [10]. 254SMO steel (6% Mo) exhibits excellent pitting resistance owing to favorable combination of alloying elements than conventional stainless steel such as 304, 316, and 316L stainless steel [11,12]. However, high amounts of Mo and Cr in 254SMO cause harmful brittle precipitations such as Chi phase, sigma phase, metal carbides, and laves phase, probably negatively affecting the corrosion resistance and passivation [2,3,13].

To prepare a passive film strong enough to bear harsh conditions, addition of boron into steel was found to be effective [14]. Addition of boron into steel decreases the intergranular corrosion rate and significantly decreases the reactivation rate in a dilute sulfuric acid medium, but the repair capacity of passive film is improved [15]. The presence of boron in alloys exhibited a beneficial effect on the pitting resistance of steel, and boron hindered $Cr_{23}C_6$ precipitation. Thus, boron exhibited significant beneficial effect on the intergranular corrosion resistance of steel as well [16]. Boron is mainly located at the grain boundaries in the steel and creates $Fe_{23}(B,C)_6$ with a very small grain size and eliminates the carbides present there [17]. Furthermore, borated stainless steel shows good passive film strength and repassivation ability [18]. However, the effect of boron on the transpassive film stability of 254SMO in FGD solutions has been rarely studied.

In this study, boron was used in parts per millions (40 ppm) in 254 SMO stainless steel. It is explained how boron successfully hinders the erosion of grain boundary and initiation of pits and improves the repassivation ability. All the experiments were systematically conducted at different temperatures.

2. EXPERIMENTAL PROCEDURE

2.1. Materials and solutions

Superaustenitic stainless steel 254 SMO was smelted using a vacuum induction furnace according to the ASTM A312 composition standard in Taiyuan Iron and Steel Group Co., Ltd. (TISCO). The main composition of both the steel samples is shown in Table 1. Then, a 12-mm-thick steel sheet was hot rolled at 1250 ℃ from the obtained ingot. To prepare specimen samples, 15×15×3 mm square pieces were cut using a wire cutter from the 12-mm-thick steel sheet, and then solid solution heat

treatment was done at 1220 ℃ for 5 h, and water quenched. After embedding (mounting press) in a hard thermosetting epoxy resin, each sample was mechanically ground with sandpapers, grit 120 to 2500, and then polished until a mirror-like surface was obtained. Moreover, prior to further experiments, all the samples were ultrasonically cleaned with distilled water and ethanol each time.

Table 1. Chemical composition (wt %) of the samples used for experiments.

No.	C	Si	Mn	P	S	Cr	Ni	Mo	Cu	N	B
254SMO-0B	0.010	0.610	0.430	0.015	0.001	20.180	18.000	6.000	0.690	0.193	0.000
254SMO-40B	0.014	0.620	0.540	0.014	0.006	20.150	18.110	6.120	0.720	0.200	0.004

2.2 Electrochemical measurements

A simulated FGD solution was prepared for electrochemical experiments. The chemical composition of FGD solution is 16.9 vol% of H_2SO_4 and 0.35 vol% of HCl. This "simulated FGD solution" is considered to be the optimum representative of corrosive environment in Korea FGD facilities [5,19]. Electrochemical measurements were carried out in FGD solutions under atmospheric pressure at three different temperatures. The simulated FGD solution was used in a three-electrode corrosion cell as an electrolyte. One of the electrodes was a saturated calomel electrode (SCE) that acted as a reference electrode; the second electrode was a platinum foil that acted as a counter electrode; the third electrode was the working electrode (sample/specimen) with an exposure area of 1 cm^2. Prior to the measurements, the working electrodes were initially potentiostatically reduced at –0.6 V for 10 min to remove the air-formed oxides [20]. Anodic polarization experiments were started after stabilizing the open circuit potential (OCP) for 30 min. Polarization curves were potentiodynamically recorded at 0.5 mVs^{-1} at three different temperatures: room temperature, 40 ℃, and60 ℃. The corrosion rate and corrosion current densities (I_o) were obtained using a software CS studio CView2. Pitting potential and passive regions were evaluated from the polarization curves.

Just after the polarization, the surface of each sample was examined by scanning electron microscopy (SEM) at different magnifications. To properly visualize the grain boundary erosion/pitting depths by optical microscopy, the side sections of each sample was chemically etched with Aqua Regia for 30 s. The sides of the samples were polished until a mirror-like surface was obtained for cross-sectional view and analyzed using optical microstructures.

Before the electrochemical measurements, an OCP curve was obtained for 30 min in the same electrolyte (simulated FGD solution) for analyzing the electrochemical behavior of passive film developed on the surface of samples [21,22]. Electrochemical impedance spectroscopy (EIS) measurements were carried out in the frequency range from 0.01 Hz to 100 kHz with a signal amplitude perturbation voltage of 10 mV of AC potential. Then, the EIS fitted data were analyzed using a commercial software ZSimpWin. After the EIS, Mott-Schottky analysis was carried out at 1 kHz in the potential range of –1.0 V to 1.0 V.

To evaluate the passive film stability of both categories of specimens (borated nonborated), X-ray photoelectron spectroscopy (XPS) was conducted at 60 ℃ for 2 h passivation. Then, an XPS depth profile study was conducted, and both categories of samples were compared

3. RESULTS AND DISCUSSION

3.1. Potentiodynamic Polarization and surface morphology

Figs. 1 and 2 show the polarization curves and surface morphology micrographs of both types of specimens of 254 SMO stainless steel with boron and without boron performed in a simulated FGD solution. The trends of all the curves are the same at each temperature. As shown in Fig. 1, neither an active current peak nor a Flade potential is observed, indicating that the metal is passivated due to the formation of an oxide film during the test [9,22]. By comparing the corrosion current densities (I_o) as shown in Table 2, it was found that the sample with boron has a lower corrosion density. Previous studies showed that corrosion densities (I_o) represent the dissolution rate of passive film formed during passivation. Therefore, higher current densities lead to a higher dissolution rate or porosity of the passive film [23]. This indicates less protective ability of the passive film, as shown in Fig. 2. Moreover, a comparison (Table 2) of corrosion rate also clearly shows that borated samples have a lower rate of corrosion. Also, the pitting potential (E_p) of borated samples is higher in comparison, which can be compared from the surface morphology micrographs (Fig. 2 (a,b)). The Micrographs show that samples with boron have negligible pit initiation sites and grain boundary deterioration.

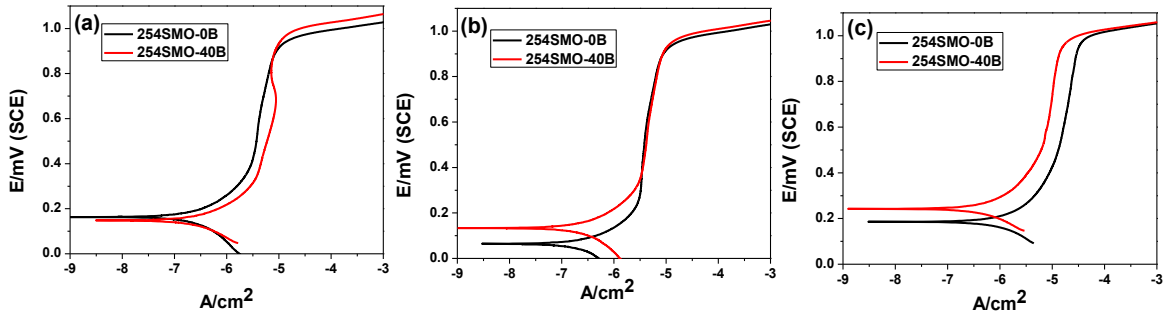

Figure 1. Potentiodynamic polarization curves of the 254SMO stainless steel with and without Boron, in the simulated FGD solution: (a) at (RT) room temperature, (b) 40 ℃ (c) 60 ℃.

Table 2. Fitted data of potentiodynamic polarization curves at three different temperatures. RT (Room temperature), 40 ℃, 60℃.

Sample/Tem	I_o(Amp/cm^{-2})	E_o(mV)	Corr-rate(mmPY)	E_p(mV)
254-0B-RT	1.203E-06	0.162	0.028	0.957±0.025
254-40B-RT	4.598E-07	0.148	0.010	0.989±0.025
254-0B-40℃	1.470E-06	0.063	0.034	0.943±0.025
254-40B-40℃	8.091E-07	0.133	0.019	0.955±0.025

254-0B-60℃	3.645E-06	0.185	0.085	0.985±0.025
254-40B-60℃	1.177E-06	0.242	0.027	1.196±0.025

Other studies obtained the same results in anodic polarization experiments in a sulfuric acid solution: Borated steel exhibited better uniform corrosion resistance and passivation properties, and boron significantly improved the corrosion resistance [16,22].

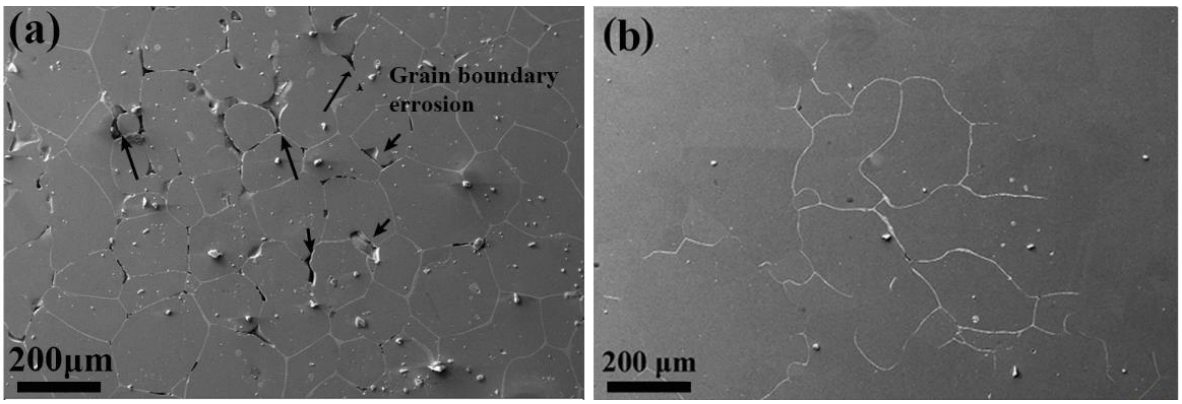

Figure 2. Surface morphology micrographs (SEM) after polarization 60℃ (a) 254SMO-0B, (b) 254SMO-40B

The reason for reducing the nucleation of pitting by adding boron is that a microstructure comprised of dispersion of boride precipitates rich in chromium in an austenitic matrix is good for corrosion resistance [24]; therefore, precipitates rich in chromium borides instead of carbides avoid pitting corrosion. Robinson and Scurr [16] studied the intergranular corrosion of borated stainless steel and discovered a greater resistance to intergranular corrosion in a sensitized state, as boron delays the formation of chromium carbide net. Carbide precipitates have high strain energy sites at the grain boundary, and boron moves these high-energy sites, thus delaying precipitations [18]. Boron can enhance the strength of grain boundary, and its segregation enhances intergranular cohesion [25]. Here, in nonborated steel, the absence of boron leads to more transpassive dissolution rate and grain boundary erosion in an FGD solution.

3.2. Electrochemical impedance spectroscopy (EIS)

Further information about hindrance to dissolution mechanism by boron addition was obtained by EIS. EIS measurements are shown in the form of Nyquist plots (Fig. 3(a)), exhibiting a semicircle in the simulated FGD solution. The diameter of the semicircle of curves with boron in the Nyquist diagrams is higher than that of the curves of nonborated samples, indicating a higher corrosion resistance [20]. Therefore, it can be assumed that the passivation on boron containing samples was stronger and stable.

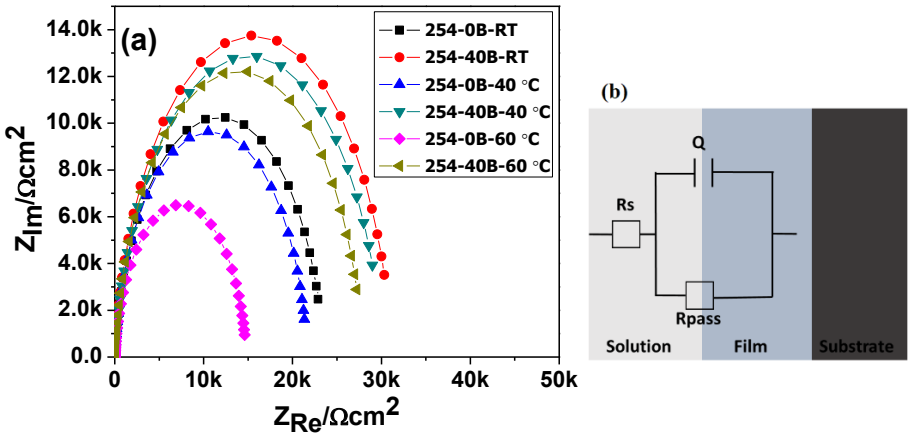

Figure 3. (a) Nyquist plot of 254SMO stainless steel with and without Boron: at Room temperature (RT), 40 ℃ and 60 ℃. (b) Electrical equivalent circuit used to fit Impedance data

This electrochemical response in the EIS experiments of these samples was well simulated with the electrical equivalent circuit (EEC) shown in Fig. 3(b). This EEC for EIS fitting data was obtained to quantify the electrochemical parameters, where the solution resistance is represented by Rs and the passive film layer or rust layer resistance is represented by Rpass. The circuit also contains capacitance Q (constant-phase element (CPE)), allowing for depressed semicircles [26]. C represents the capacitive behavior of the passive film formed, coupled with a resistance owing to the ionic paths through the oxide film Rpass. Four different equivalent circuits can be used to describe the electrochemical behaviors/reactions at the junction of electrode/electrolyte during passivation [9].

Table 3. Fitting data of Nyquist plot

Sample/℃	R_s (Ω cm^2)	Q (Ω^{-1} s^{-n} cm^2)	n	R_{pass} (Ω cm^2)
254-0B-RT	1.905	5.913E-5	0.914	2.349E4
254-40B-RT	1.895	4.848E-5	0.920	3.118E4
254-0B-40℃	1.553	4.616E-5	0.926	2.165E4
254-40b-40℃	1.654	5.605E-5	0.899	3.017E4
254-0B-60℃	1.746	5.689E-5	0.919	1.479E4
254-40B-60℃	1.499	4.916E-5	0.916	2.792E4

Table 3 shows the fitting data according to the EEC given above. The Rpass value of each borated sample is higher than that of nonborated specimens, indicating that the samples with boron has a stable passive film and much better corrosion resistance at each temperature. These results are consistent with the previous results of potentiodynamic polarization that boron hinders the dissolution of passive film and makes it compact. In addition, it is well known that if the passive film is strong and stable, than less general corrosion occurs.

3.3. Mott-Schottky analysis

Mott-Schottky measurements are usually carried out to characterize the properties of semiconducting behavior and charge density carriers of a passive film [9]. To measure the space charge capacitance of *N*-type semiconducting phenomenon of a passive film, or to measure the donor densities of a passive film, an equation can be used according to Mott-Schottky theory as follows:

$$C^{-2} = C_H^{-2} + C_{SC}^{-2} = \frac{2}{\varepsilon_s \varepsilon_o q N_D}\left(E - E_{fb} - \frac{kT}{e}\right)$$

where ε_o is the vacuum permittivity; ε_s is the dielectric constant of specimen; e is the electron charge; k is the Boltzmann constant (1.38×10^{-23} JK^{-1}); N_D is donor density [27]. The Mott-Schottky curves were recorded (Fig. 4) for passive films formed on both the categories of samples, borated and nonborated in a simulated FGD solution. The trend of each curve is almost the same. *N*-type positive slopes of semiconductor regions are shown, from where donor densities are cation interstitials or oxygen vacancies [9]. Previous studies reported about the slops, which have steeper or higher peaks and show lesser generation of donors or acceptors. Moreover, the lower peaks or less steep curves show that there must be a high generation of donor species [28]. Therefore, in this case, the samples with boron show high curves or steeper peaks in the regions of *N*-type. This shows that owing to boron, less cation vacancies are present; hence, the passive film is stable and not perforated because of the generation of these densities. At room temperature and 40 °C, from 0.0 V to nearly 0.4 V, both categories of samples showed the same performance, but at 60 °C, the performances are different.

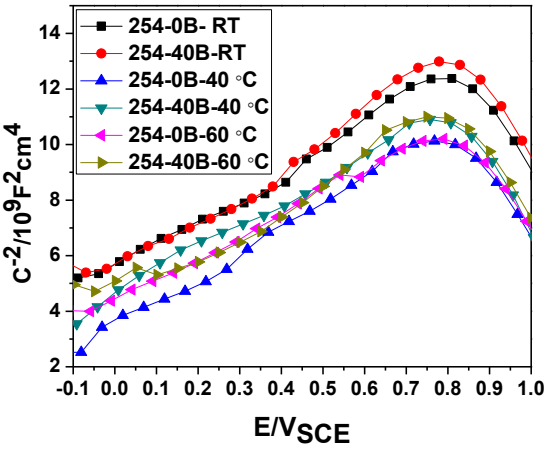

Figure 4. Mott-schottky plots of 254SMO stainless steel with and without Boron: at room temperature (RT), 40 °C and 60 °C.

All the potential profiles above –0.1 V_{SCE} are nonlinear. The nonlinearity can be attributed to the presence of donor levels in the passive films [28]. The data (Table 4) of donor densities could be enough to explain the passive film behavior, as some studies reported that a high donor density is harmful to the stability of a passive film, and the electrochemical reaction occurring at a solution/metal interface also increased. Thus, this process favored the dissolution of passive film [23]. Furthermore, N_D represents the adsorption affinity of chloride ions in the passive film. Thus, it can feature the pit nucleation ability

of passive film [28]. These calculated carrier donor densities showed that the samples with boron generated less densities at each temperature, i.e., the passive film on boron containing specimens remains more stable and less sensitive to pitting nucleation compared to nonborated samples, where the passive film becomes defective, perforated, disordered, and more sensitive to pitting nucleation due to more generation of densities.

Table 4. Calculated carrier density for Mott-Schottky plots in figure 5

Sample	N_D (10^{12} at cm^3)
254-0B-RT	8.545
254-40B-RT	7.452
254-0B-40℃	11.00
254-40B-40℃	10.52
254-0B-60℃	11.54
254-40B-60℃	10.79

3.4. Grain boundary erosion analysis

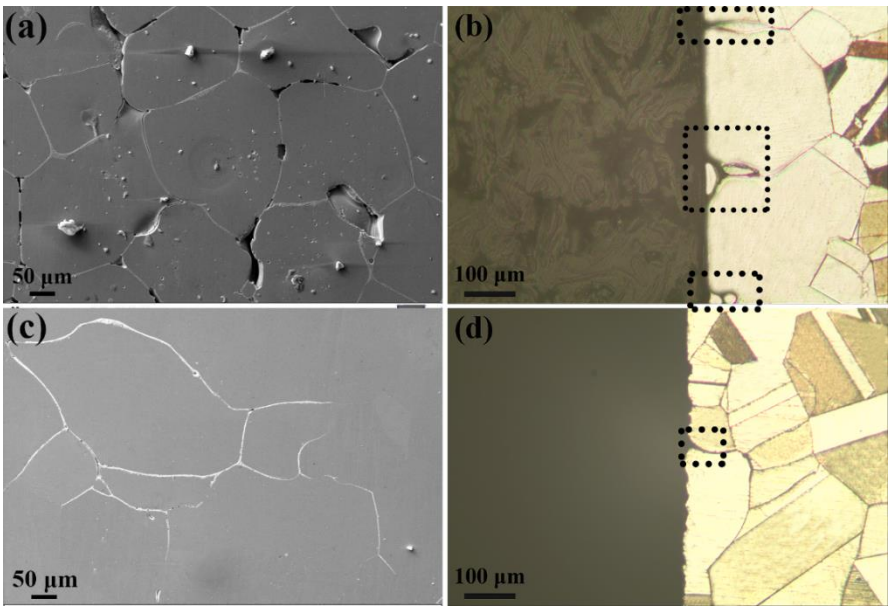

Figure 5. After polarization at 60 ℃ a comparison of pits/grain erosion depth: (a, b) 254SMO-0B, (c, d) 254SMO-40B (b, d) side view of cross section of (a, c) respectively

The SEM microstructures obtained after polarization at 60 ℃ could be analyzed from Fig. 2. Here, the positive effect of boron over grain erosion or pit penetration is explained in grain erosion/pitting depth analysis. In the comparison of (Fig. 5 b) without boron and (Fig. 5 d) with boron (side views of the center cut samples), clearly the pits present in sample without boron have penetrated more in depth along the three points of grain boundaries.

In addition, after 60 ℃ polarization, the sample without boron Fig. 5(a) and its side view (b) has a large number of pits due to huge erosion of grains (shown in dotted rectangles). However, the sample

with boron Fig. 5(c) and its side view Fig. 5(d) show less grain erosion damage. The number of pits or perforation into grains is higher at a higher temperature because the ions present inside the passive film are aggressive to mitigate. Moreover, at high temperatures, the dissolution rate also increased [9,29]. Therefore, in the FGD solution, the chloride ions and sulfide ions are more aggressive to destroy the passive layers at high temperatures. In the solution, chlorides are very corrosive due to their small size, high mobility, and high dispersion solubility [30]. Under a high potential difference, Cl^- ions diffuse through the protective film, thus displacing H_2O and OH groups and inducing the localized breakdown of passive layer [31]. Therefore, the diffusion of these ions can generate grain erosion damage or pits and cavities, further leading to pitting corrosion, which is the formation of cavities in a passive metal [21]. O'Laoire C [32] found similar results during the acid passivation of stainless steel.

Significant difference was observed in the occurrence of grain erosion damage in both types of samples, especially after polarization. Obviously, the samples without boron have a higher concentration of segregates in the grains, resulting in pits and grain erosion/damage. Energy-dispersive X-ray spectroscopic analysis was conducted (Fig. 6) on the sample polarized at 60 ℃ to determine the composition of grain segregations. Phosphorous was found to be the main component of grain boundary segregation, causing intergranular corrosion and grain boundary erosion [33]. Boron reduces the strain energy in grain boundaries as it diffuses into the lattice imperfections. The areas with less strain energy cannot be corrosion/pit initiation sites; therefore, the addition of boron lowers the high-energy sites. In short, it resists the erosion of grains [14,18]. When the lattice imperfections are filled, excess boron precipitates, thus producing a boron-rich grain boundary, and boron lowers the energy level of potential nuclei and thus lowers the probability for nucleation [34].

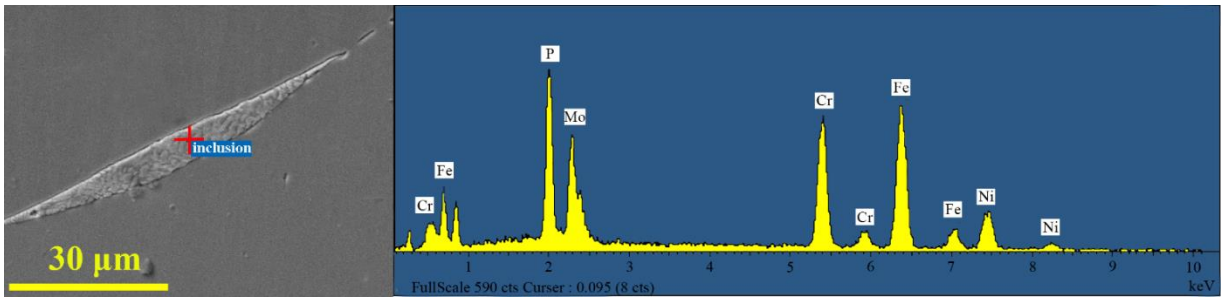

Figure 6. EDS analysis of microstructure of 254 SMO after polarization at 60℃

Fig. 7 shows a three-dimensional schematic diagram, which simply shows the top surface and side cross-section of 254 SMO stainless steel after polarization at 60 ℃ in a simulated solution of FGD. This diagram shows how and where the pits are initiated, and where the corrosion occurs mostly. The sample without boron has a higher number of pit initiation sites/inclusion and intermittent corrosion compared to the sample with boron. Intermittent corrosion or segregation, which was found along the grain boundaries or three joints of the grains, had phosphorous element, leading these segregations to initiate pit formations. However, after the addition of boron, this segregation decreased, eventually decreasing the size and number of pitting phenomena.

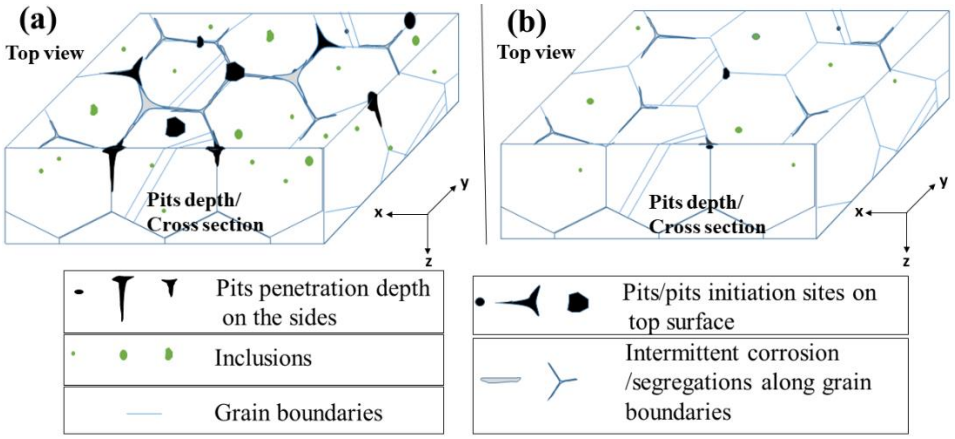

Figure 7. A schematic diagram of 254SMO stainless steel after polarization in FGD solution: (a) top and cross section view of 254SMO-0B (b) top and cross section view of 254SMO-40B

3.5. Characteristics of Surface Passive Film

XPS measurements were conducted after a passive film was formed in the passive region, which is believed to be responsible for the corrosion resistance of material. Therefore, passivation was conducted at 0.6 V passive potential for 2 h at 60 ℃. After obtaining the data, XPSPEAK version 4.1 software was used for curve fitting. The software was set on the tail function of Shirley background subtraction and Gaussian-Lorentzian, for achieving better spectra fitting. For a comparison of the detailed change in the composition, the spectra of Cr and Mo oxide films grown on both types (borated and nonborated) of samples are shown in Fig. 9. Fig. 8 shows the optical microstructures of borated and nonborated samples just after polarization at 60 ℃.

Table 5. The binding energies considered for fitting [35].

Element	Peak	Species	Binding energies
Cr	$2p_{3/2}$	Cr_{met}	574.1
		Cr_2O_3	576.3
		$Cr(OH)_3$	577.3
Fe	$2p_{3/2}$	Fe_{met}	707.0
		Fe^{2+}	709.4
		Fe^{3+}	711.0
Mo	$3d_{5/2}$	Mo_{met}	227.4
		Mo^{4+}	230.2
		Mo^{6+}	232.2
	$3d_{3/2}$	Mo_{met}	230.9
		Mo^{4+}	233.4
		Mo^{6+}	235.1
Ni	$2p_{3/2}$	Ni_{met}	852.8
		NiO	854.3
		$Ni(OH)_2$	855.6
O	1s	O^{2-}	530.2
		OH^-	531.8
		H_2O	533.0

The nonborated sample (Fig. 8a) exhibits a damaged/perforated passive surface, but the borated sample (Fig. 8b) shows thick passivation. The XPS spectral results indicate that the presence of Cr2p, Fe2p, Mo3d, and Ni 2p varied with the addition of boron. Table 5 shows the binding energies of each element. These data were used for studying XPS peaks and passive film depth.

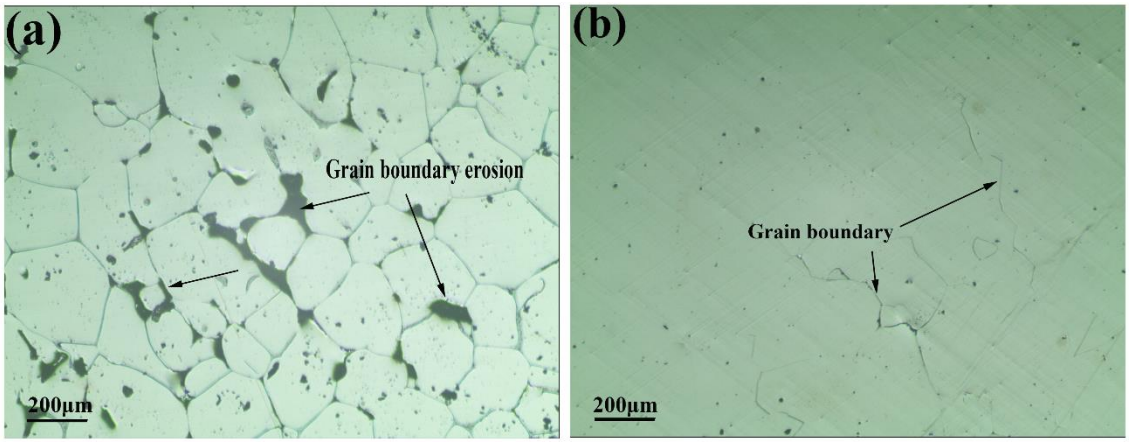

Figure 8. Optical microstructures of 254SMO stainless steel after polarization at 60°C (a) 254SMO-0B (b) 254SMO-40B

In Fig. 9 (b), the deconvolution results show that a sample with boron is enriched with Cr oxides. Corrosion rate is strongly affected by the content ratio of chromium oxide in the passive layers. Here, it can be said that the boron helps in the presence of Cr_2O_3 within the passive film. The passivation behavior contrasts the corrosion rates of metal alloys [31]. It is well known that chromium oxides are essential on the surface of steels for corrosion resistance and passive film stability [33]. Molybdenum species concentration in the outermost layer was found to be almost the same in both types of samples.

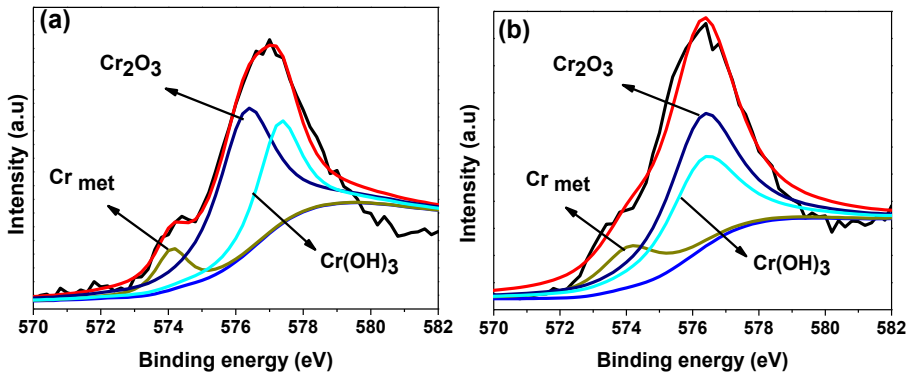

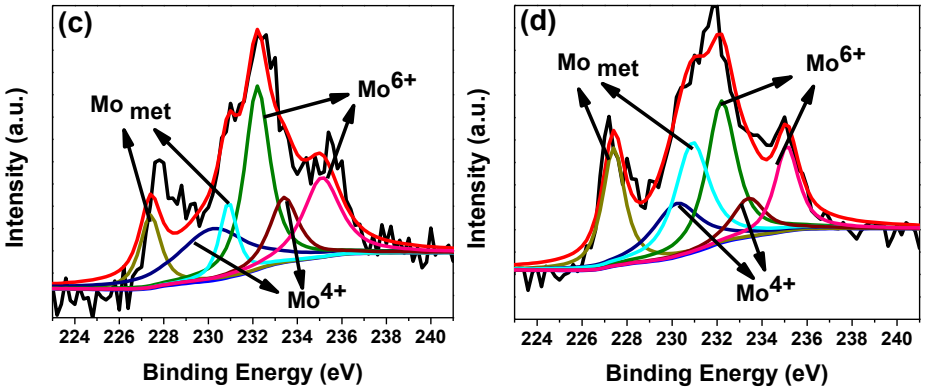

Figure 9. XPS spectra of the passive film formed on 254SMO in the simulated FGD solution. (a) XPS spectra of $Cr2p_{3/2}$ -254SMO-0B (b) XPS spectra of $Cr2p_{3/2}$ -254SMO-40B (c) XPS spectra of Mo $3d_{5/2}$-254SMO-0B (d) XPS spectra of Mo $3d_{5/2}$-254SMO-0B

3.6. Cationic Fraction

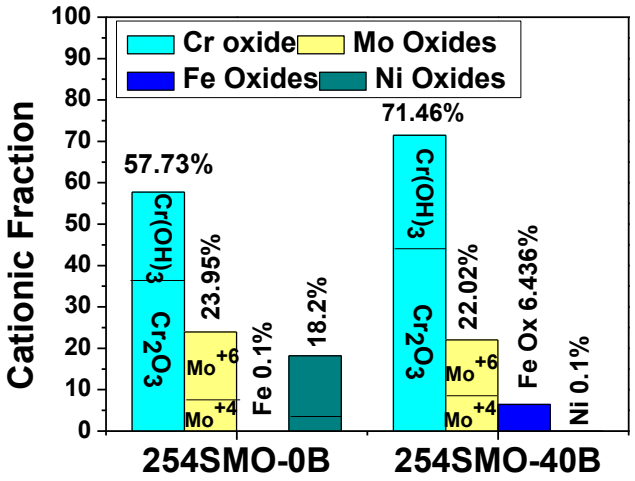

Figure 10. The XPS cationic fraction (C_x) in the passive film of 254SMO after 2h passivation at 60°C temperature.

Cationic fraction is also used to characterize the composition of a passive film. Fig. 10 shows the cationic fraction of Cr, Fe, Mo, and Ni for both categories of sample in the passive film calculated using the following formula [36]:

$$C_X = \frac{Ix/Sx}{\sum Ii/Si}$$

where C_x is the atomic percentage; I_x is the peak intensity corresponding to the area of elements in the passive film; S_x is the sensitivity factor based on the XPS instrument. In this study, the sensitivity factors of Cr, Mo, Fe, and Ni are 2.201, 2.686, 2.867, and 3.653, respectively [35].

These quantitative results suggest that in the case of borated samples, the primary constituent of passive film is Cr oxides. Passive film comprised of Cr oxides is a good sign for the strengthening and

compactness of a film. These results reinforce the idea of addition of boron into 254 SMO stainless steel, as such addition of boron successfully improved the Cr content in the surface of passive film.

3.7. XPS depth profiles

First, the atomic concentration was measured to determine the detailed chemical composition of alloying elements distributed in the passive film, as shown in Fig. 11. Table 6 shows the concentration of elements during the initial stage of sputtering. The data show that the percentage of Cr element is less, and the percentage of Fe element is higher during the initial sputtering stages in the sample with boron, i.e., the number of Cr elements that changed into chromium oxide must be higher than the number of Fe oxide compounds in the boron added sample (Fig. 11 (b)). Concentrations of both the samples show variations in passive film composition only up to 30 s sputtering time. After this sputtering time, the proportion of Cr and Fe becomes almost constant and approaches the alloying proportion, i.e., a film/metal interface exists.

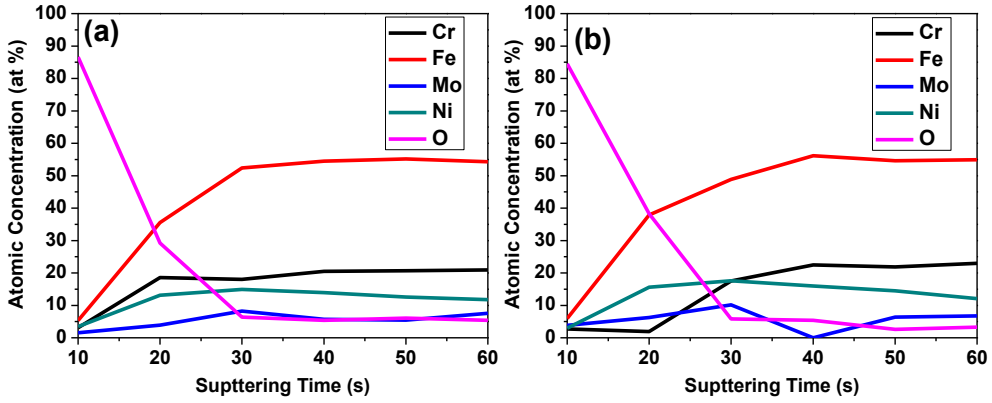

Figure 11. XPS sputtering depth profiles of the distribution of the alloyed elements of 254SMO stainless steel (a) 254SMO-0B (b) 254SMO-40B

Table 6. Concentration of the elements during the initial stage of the sputtering (10s)

Element	Cr (at. %)	Fe (at. %)	Mo (at. %)	Ni (at. %)	O (at. %)
254SMO-0B	3.07	5.3	1.53	3.48	86.6
254SMO-40B	2.72	5.929	3.81	2.96	84.55

Fig. 12 shows the sputtering depth profiles of oxides in the passive film. In the outermost layers, concentrations of Cr_2O_3 and $Cr(OH)_3$ in the boron contaminated sample (Fig. 12 (b)) are higher compare to the sample without boron (Fig. 12 (a)). In the innermost layers, the concentration of Fe oxides decreases. This indicates that the sample with boron has a compact and strong passive film. Moreover, the concentration of Mo species in the innermost layer of boron added sample (Fig. 12 (b)) is higher, and it is proposed that Mo mitigates the breakdown of passive film and promotes the repairability of passive film, improving the chemical stability, homogeneity, and compactness of passive film [37,38].

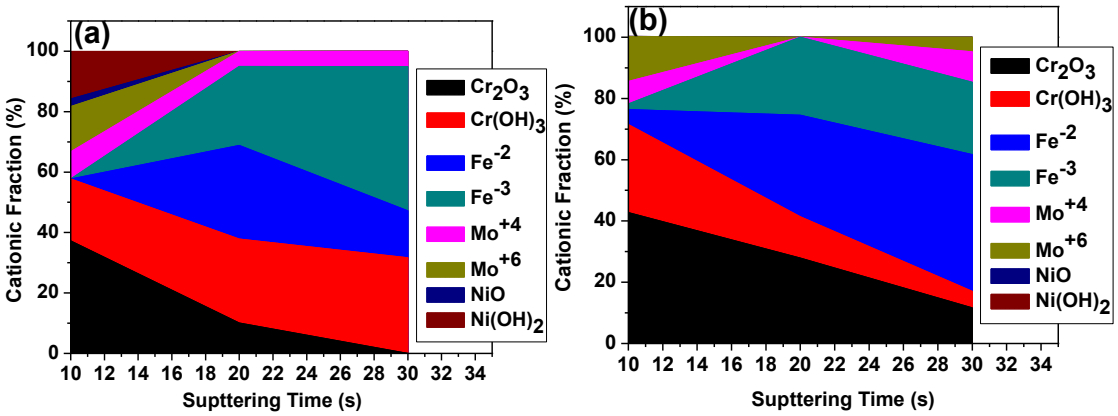

Figure 12. XPS sputtering depth profiles of the oxides in the passive film of 254SMO stainless steel (a) S31254-0B (b) S31254-40B

Fig. 13 shows the XPS spectra of O_{1s} of both types of samples and their corresponding fractions. The XPS spectra and fraction for boron added sample (Fig. 13(b, d)) show that there is less O^{-2} and more H_2O. Previous studies reported that the bound water in a passive film acts as a self-repairing agent of the passive film. Moreover, the bound water in the passive film acts as an effective species to capture the dissolving metal ions and forms a new passive film against further attack by the surrounding species [39]. Therefore, it can be concluded that boron added samples have a protective passive film.

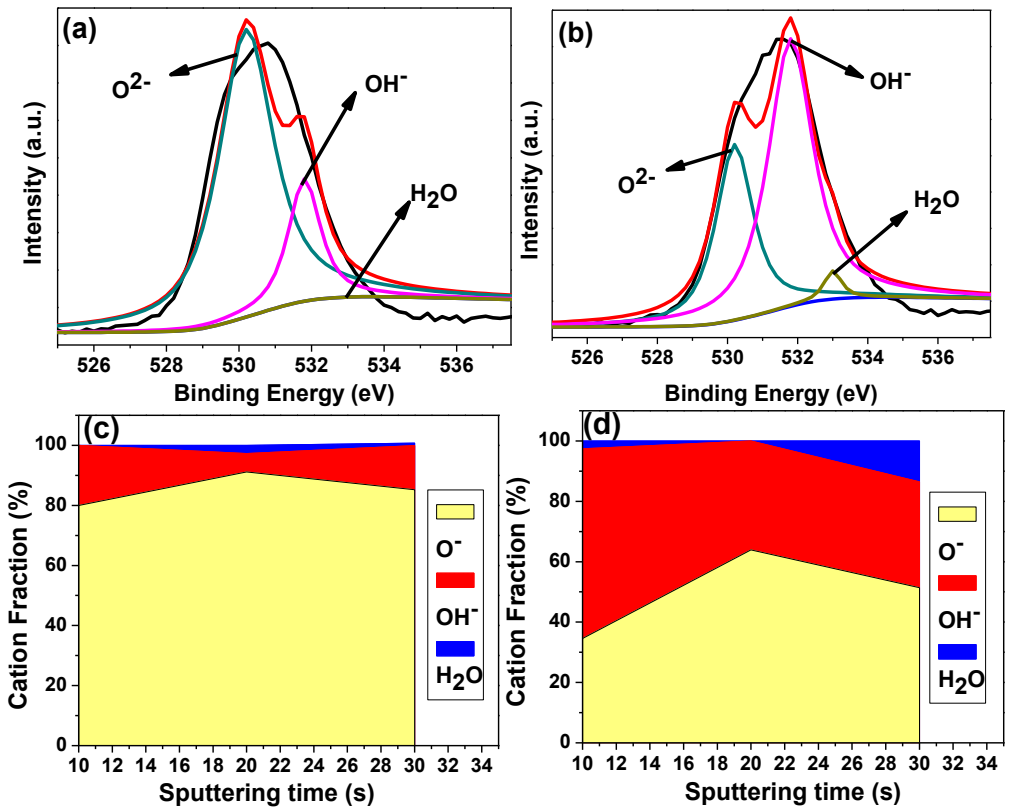

Figure 13. (a) and (c) XPS spectra of O_{1s} and corresponding fraction of 254SMO-0B respectively, (b) and (d) XPS spectra of O_{1s} and corresponding fraction of 254SMO-40B respectively

4. CONCLUSION

Grain boundary erosion and passivation of borated 254 SMO stainless steel in a simulated FGD solution were evaluated using different techniques. The results are as follows:

1. The results of potentiodynamic, EIS, and Mott Schottky analysis at room temperature, 40 ℃, and 60 ℃ show that the addition of boron decreased the corrosion current densities and hindered the dissolution rate of passive films. The semiconducting species (donor densities) also decreased.

2. The optical and SEM microstructures show that borated samples did not suffer from grain boundary erosion/perforation and pitting sites. The EDS analysis shows that the grain boundary segregation of nonborated samples comprised of phosphorous, which caused pits and inclusions and increased the dissolution rate of passive film.

3. The XPS results and depth profiles after passivation at 60 ℃ corroborate the electrochemical and SEM results, as the results show that the addition of boron enriched the metal with Cr and Mo species both in the outer and inner layers of passive film and decreased the content of Fe_2O_3 and $Fe(OH)_2$ in the passive film composition.

4. Bound water was found in the passive film of borated sample, which is also the reason of strengthening passive film.

ACKNOWLEDGEMENTS
The present work was financially supported by National Natural Science Foundation of China (Grant No. U1860204, No 51871159), the Natural Science Foundation of Shanxi Province (Grant No. 201801D221125, No. 201601D202033, No. 201601D202034) and Innovation Project for Graduate Education of Shanxi province (Grant No. 2018SY012).

References

1. Y. Han, H. Wu, W. Zhang, D. Zou, G. Liu and G. Qiao, *Mater. Des.,* 69(2015)230.
2. J. Bai, Y. Cui, J. Wang, N. Dong, M.S. Qurashi, H. Wei and P. Han, *J. Iron. Steel Res. Int*., (2018).
3. J. Bai, Y. Cui, J. Wang, N. Dong, M.S. Qurashi, H. Wei and P. Han, *Metals,* 8(2018)497.
4. M. A. Anjos, R. Vilar and Y.Y. Qiu, *Surf. Coat. Technol.,* 92(1997)142.
5. W.–S. Ji, Y.–W Jang and J.-G. Kim, *Met. Mater. Int.,* 17(2011)463.
6. F. Ferrer, T. Faure, J. Goudiakas and E. Andrès, *Corros. Sci.,* 44(2002)1529.
7. Z. B. Wang, H. X. Hu, C. B. Liu and Y. G. Zheng, *Electrochim. Acta,* 135(2014)526.
8. C. Escrivà-Cerdán, E. Blasco-Tamarit, D. M. García-García, J. García-Antón and A. Guenbour, *Corros. Sci.,* 56(2012)114.
9. Z. Cui, L. Wang, H. Ni, W. Hao, C. Man, S. Chen and X. Li, *Corros. Sci.,* 118(2017)31.
10. M. Bojinov, G. Fabricius and P. Kinnunen, *Electrochim. Acta*, 45(2000)2791.
11. E. A. Abd El Meguid and A. A. Abd El Latif, *Corros. Sci.,* 49(2007)263.
12. E.A. Abd El Meguid and A. A. Abd El Latif, *Corros. Sci.,* 46(2004)2431.
13. J. Zhang, S. Li, F.-Z. Xuan and F. Yang, *Mater. Sci. Eng., A,* 622(2015)146.
14. M. S. Qurashi, Y. Cui, J. Wang, N. Dong and J. Bai, *Int. J. Electrochem. Sci.,* 14(2019)10642.
15. T. M. Guo, D. C. Zhang, Z. Hui, C. S. Han and L. M. Zhao, *Adv. Mater. Res.,* 415(2011)800.
16. F.P.A. Robinson and W. G. Scurr, *Corrosion*. 33(1977)408.
17. H. Düzcükoğlu and S. Çetintürk, *IJMMM.,* 3(2015)1793.
18. J. Wang, Y. Cui, J. Bai, N. Dong, Y. Liu, C. Zhang and P. Han, *Mater. Lett.,* 252(2019)60.

19. D. P. Le, W.S. Ji, J. G. Kim, K. J. Jeong and S. H. Lee. *Corros. Sci.,* 50(2008)1195.
20. H. Luo, C.F. Dong, X.G. Li and K. Xiao. *Electrochim. Acta,* 64(2012)211.
21. M. BenSalah, R. Sabot, E. Triki, L. Dhouibi, P. Refait and M. Jeannin, *Corros. Sci.,* 86(2014)61.
22. N. S. Bharasi, M.G. Pujar, S. Nirmal, C. Mallika, U. K Mudali, and P.C. Angelo. *J. Mater. Eng. Perform.,* 25(2016)2786.
23. M.B. Salah, R. Sabot, P. Refait, I. Liascukiene, C. Méthivier, J. Landoulsi, L.Dhouibi and M. Jeannin, *Corros. Sci.,* 99(2015)320.
24. C.V. Robino and M.J. Cieslak, *Metall. Mater. Trans.* A, 26(1995)1673.
25. Z. W. Zhang, C. T. Liu, S. Guo, J. L. Cheng and G. Chen, *Mater. Sci. Eng*., A, 528(2011)855.
26. G. B. Zou, W. Shi, S. Xiang and X. M. Ji, *RSC Adv.*, 8(2018)2811.
27. L. Jinlong, T. X. Liang, L. Dong and C. Wang, *Corros. Sci*.,104(2016)144.
28. L. Jae-Bong and Y. Sang-In, *Mater. Chem. Phys.*, 122(2010)194.
29. M. Bojinov, G. Fabricius, T. Laitinen, and T. Saario, *J. Electrochem. Soc.,* 145(1998)2043.
30. M.A.M Ibrahim, S.S. Abd El Rehim and M.M. Hamza, *Mater. Chem. Phys.*,115(2009)80.
31. T. L. Roland, *J. Mater. Res. Technol*., 2018.
32. C. O'Laoire, B. Timmins, L. Kremer, J. D. Holmes and M. A. Morris, *Anal. Lett.*, 39(2006)2255.
33. G.-L. Song, C.-N. Cao and H.-C. Lin, *Corros. Sci*., 36(1994)165.
34. K. N. Kim, L. M. Pan, J. P. Lin, Y. L.Wang, Z. Lin and G. L. Chen, *J. Magn. Magn. Mater*., 277(2004)331.
35. J.F. Moulder, W.F. Stickle, P.E. Sobol and K.D. Bomben, Handbook of X-ray Photoelectron Spectroscopy, Perkin–Elmer, Physical Electronic Division, Eden Praire, MN,(1992).
36. C. T. Liu, J. K. Wu, *Corros. Sci.*, 49(2007)2198.
37. L. Jinlong, T. X. Liang, L. Dong and C. Wang, *Mater. Lett*., 171(2016)38.
38. H. Tian, X. Cheng, Y. Wang, C. Dong and X. Li, *Electrochim. Acta*, 267(2018)255.
39. H. Luo, X. Wang, C. Dong, K. Xiao and X. Li, *Corros. Sci.*, 124(2017)178.